This paper is published as part of a PCCP Themed Issue on:
Electronic Structures and Reaction Dynamics of Open-shell Species

Guest Editors:
Jingsong Zhang - *University of California, Riverside*
Martin Head-Gordon - *University of California, Berkeley*

Predissociation of the $A\ ^2\Sigma^+$ ($v' = 3$) state of the OH radical

Dragana Č. Radenović,[a] **André J. A. van Roij,**[a] **Shiou-Min Wu,**[a] **J. J. ter Meulen,**[a]
David H. Parker,*[a] **Mark P. J. van der Loo**[b] **and Gerrit C. Groenenboom**[b]

Predissociation of electronically excited OH $A\ ^2\Sigma^+$ ($v' = 3$) is studied using velocity-map imaging of the atomic oxygen photofragments. Fine structure yields, angular distributions and alignment parameters are obtained for the $O(^3P_J)$, $J = 2,1,0$ products. Angular distributions for the $O\ ^3P_0$ ($J = 0$) fragment, which has no angular momentum polarization, agree well with predictions from the angular distribution simulation computer routine by Kim *et al.* [*J. Chem. Phys.*, 2006, **125**, 133316] which calculates the anisotropy of photofragment recoil as a function of dissociation lifetime, excitation frequency, rotational level, and rotational constant. When angular momentum polarization (*i.e.* non-equilibrium population distributions of the magnetic sublevels) of the atomic fragments is present, the polarization sensitivity of the $O(^3P_J)$ (2 + 1) resonance enhanced multiphoton ionization (REMPI) detection scheme used to detect the $O(^3P_{2,1})$ products affects the measured angular distribution. Strong polarization effects are observed for the $O(^3P_{2,1})$ products and accounted for in a simple sudden limit model for the photodissociation. In agreement with the sudden limit predictions for pre-dissociation of OH $A\ ^2\Sigma^+$ ($v' = 3$) through the $^4\Sigma^-$ state, strongly aligned $O(^3P_2)$ is found to be the major product.

1. Introduction

The hydroxyl free radical (OH) is a key reactive species in the chemistry of the atmosphere, in combustion process and in the interstellar medium. Although hydroxyl has been the subject of a large number of theoretical and experimental studies, only a few modern collision-free experiments on OH photo-dissociation have been reported.[1–3] We have previously used imaging detection of O and H atom products to study direct one-photon photodissociation of vibrationally excited hydroxyl radicals $X\ ^2\Pi$ (v'') via the repulsive $1\ ^2\Sigma^-$ electronic state of OH and OD[1,2] while the group of Zhang[3] has used Rydberg tagging studies of H atoms from the predissociation of OH excited to the $A\ ^2\Sigma^+$ ($v' = 3$ and 4) states. Here, we use velocity-map imaging to study vector properties of the O atom product from the predissociation of the lowest rotational levels of the OH $A\ ^2\Sigma^+$ ($v' = 3$) state. Using a hexapole state selector[4] to focus and state-select the OH beam in the $X\ ^2\Pi_{3/2}$ ($v'' = 0$, $J'' = 3/2(N'' = 1)$, F_1) rotational and vibrational ground state, in combination with detection of the O atom fragments using the velocity-map imaging technique,[5] we observe direct state-to-state (pre-) dissociation of OH under collision-free conditions. Our study is complementary to that of ref. 3, where high resolution speed distributions of the H atom product were reported. We measure correlations between the OH $A\ ^2\Sigma^+ \leftarrow X\ ^2\Pi$ transition dipole, the $O(^3P)$ atom recoil, and the $O(^3P_J)$ angular momentum

polarization vectors in our experiment. This type of data provides a sensitive test of our current understanding of product atom polarization and coherence effects in the photo-dissociation dynamics of small molecules.[6] We have also recently reported[7] a similar study of A-state ($v = 0, 1,$ and 2) predissociation in the isovalent SH/SD molecules. Results for OH described in this paper will be compared with the previously obtained SH/SD results.

Production of sufficient quantities of OH free of other molecules that yield O or H photodissociation products is very challenging. In this study the obtained signal-to noise ratio was not sufficient to justify a state-of-the-art photo-dissociation approach[8] where the laser polarization is varied on a shot-to-shot basis and all possible product polarization parameters are extracted by linear combinations of images taken for a variety of experimental geometries. Instead, we use the theory described in section 2 of this paper to predict the actual shape of the images and compare those predictions with measured values.

2. Predissociation of the $A\ ^2\Sigma^+$ state of OH

Adiabatic (spin–orbit diabatic) Born–Oppenheimer (B.O.) potential-energy curves of the ground electronic state and the lower electronically excited states of OH calculated recently by van der Loo and Groenenboom[9] are shown in Fig. 1. The OH $X\ ^2\Pi$ ground state and the $1\ ^2\Sigma^-$, $1\ ^4\Pi$, and $1\ ^4\Sigma^-$ repulsive states correlate with the first dissociation limit: $O(^3P_J) + H(^2S)$, while the bound $A\ ^2\Sigma^+$ state correlates with the second dissociation limit: $O(^1D) + H(^2S)$. Optically allowed transitions can take place from the $X\ ^2\Pi$ ground state to the $A\ ^2\Sigma^+$ and $1\ ^2\Sigma^-$ states shown in the Figure.

[a] *Laser and Molecular Physics, Institute for Molecules and Materials, Radboud University Nijmegen, Heyendaalseweg 135, 6525AJ, Nijmegen, The Netherlands. E-mail: parker@science.ru.nl; Fax: +31 (0)24 3653311; Tel: +31 (0)24 3652423*
[b] *Theoretical Chemistry, Institute for Molecules and Materials, Radboud University Nijmegen, Heyendaalseweg 135, 6525AJ, Nijmegen, The Netherlands*
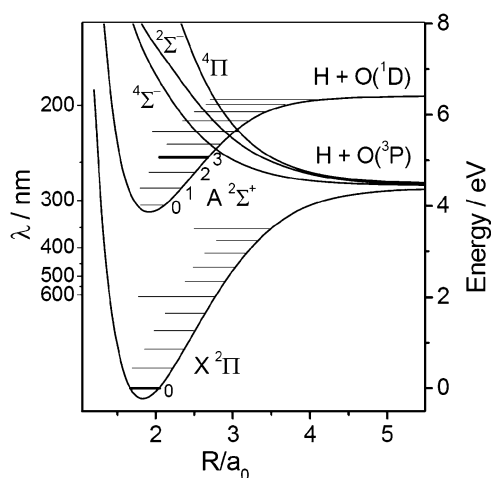
Fig. 1 Potential-energy diagram of the OH electronic states relevant for this study. The ground ($X\ ^2\Pi$) and repulsive $1^4\Sigma^-$, $1^2\Sigma^-$ and $1^4\Pi$ states correlate with the first ($O(^3P) + H(^2S)$) dissociation limit while the $A\ ^2\Sigma^+$ state correlate with the second ($O(^1D) + H(^2S)$) dissociation limit. OH is excited from $v = 0$ in the ground state to the $v = 3$ level of the A state by ultraviolet laser radiation at ~ 245 nm.

Crossing of the ($v' \geq 2$) vibrational levels of the $A\ ^2\Sigma^+$ state with the repulsive ($1\ ^4\Sigma^-$, $1\ ^2\Sigma^-$ and $1\ ^4\Pi$) states causes predissociation, which competes with fluorescence back to the ground state. Laser-induced fluorescence (LIF) *via* the $A\ ^2\Sigma^+$ state is the primary detection method for OH, and this predissociation process strongly affects the LIF detection efficiency. For a better understanding of OH predissociation, the potential-energy curves, *r*-dependent transition dipole moments, position of ro-vibrational levels, *etc.*, have been very well determined for both the $X\ ^2\Pi$ and $A\ ^2\Sigma^+$ electronic states. Predissociation occurs in the Franck–Condon region through the $1\ ^2\Sigma^-$, $1\ ^4\Pi$, and $1\ ^4\Sigma^-$ repulsive states due to spin–orbit-induced couplings.[3,10–16] The interactions between these crossing states are significant near the crossing points and determine the positions of the resonance, the linewidth, as well as the predissociation lifetime. Predissociation lifetimes of the individual rovibrational levels in the *A–X* electronic system have been extensively studied,[17–20] and all rotational levels in $v' \geq 2$ have been shown to undergo predissociation.[17] In the $v' = 2$ state the decay lifetime τ is <150 ns and in $v' = 3$ predissociation is ~ 1000 times faster, with the decay lifetime is about ~ 200 ps for low N' levels.[19,20] Higher vibrational states are expected to decay even more rapidly.[15] Recent experimental measurements[21] revealed decay lifetimes on the order of 20 ps for $N' = 0$–7 in $v' = 4$ states, which is in excellent agreement with first-principles theoretical studies.[15,16] As determined by the location of the curve crossing, the vibrational levels A($v' = 2$ and 3) predissociate predominantly *via* the $^4\Sigma^-$ state,[3,15–20] while the $v' = 4$ vibrational level decays *via* all three repulsive states: $1\ ^4\Sigma^-$, $1\ ^2\Sigma^-$ and $1\ ^4\Pi$.[3,15,16,22]

In the purely adiabatic B.O. correlation diagram the ground and three repulsive excited states ($1\ ^4\Sigma^-$, $1\ ^2\Sigma^-$, and $1\ ^4\Pi$) of OH correlate with the separated atom product states $O(^3P_J) + H(^2S)$ specified by the Ω quantum number, which is conserved between the molecular and atomic states. This means for the OH molecule

in the adiabatic B.O. limit the initially excited $1\ ^4\Sigma^-$ state dissociates following the adiabatic correlation solely to the asymptotic $O(^3P_2)$ products, while the $1\ ^2\Sigma^-$ and $1\ ^4\Pi$ repulsive states adiabatically correlate with $O(^3P_0)$ and $O(^3P_1)$ products, respectively (see Fig. 4 from ref. 13). The O atom fine structure branching ratio is thus a direct indicator of the type of dynamics taking place.

Branching ratios for the $O(^3P_J)$ fine structure following OH A-state predissociation were investigated in detail by Parlant and Yarkony[16] using multichannel scattering theory based on potential-energy curves, spin–orbit couplings, and Coriolis couplings, determined from multi-reference configuration interaction wave functions. They computed the predissociation rates of the individual OH ($A\ ^2\Sigma^+$, v', N', F_1/F_2) levels and the fine-structure state populations of the $O(^3P_J)$ product, and concluded that the photo-predissociation dynamics of OH and the $O(^3P_J)$ spin–orbit branching fractions is affected by the:

(i) Initial partitioning of flux on the three dissociative states $1\ ^4\Sigma^-$, $1\ ^2\Sigma^-$ and $1\ ^4\Pi$ determined by the spin–orbit interaction at the crossing points.

(ii) Redistribution—and interferences—of the molecular amplitudes onto atomic amplitudes through the frame transformation. The scrambling of the initial fluxes in the recoupling zone is less important because of the rapid traversal of this region due to the large dissociation kinetic energy.

Parlant and Yarkony[16] also investigated coherence effects in the photodissociation process, and compared the predictions for incoherent excitation *versus* a full quantum treatment, and, in addition, evaluated the validity of the 'sudden limit' model for OH predissociation. For the low v',N' states we study here ($v' = 3$, $N' = 0$–2) they showed that a single ($1\ ^4\Sigma^-$) state approximation without coherence effects, evaluated in the sudden limit should be appropriate. In the following section we will use the sudden limit model to predict product angular momentum alignment effects in the molecular frame for photodissociation of OH *via* the $1\ ^4\Sigma^-$ state.

2.1 Photodissociation *via* the $1\ ^4\Sigma^-$ state in the sudden limit

Because curve crossing with the lowest, $1\ ^4\Sigma^-$, repulsive state occurs several thousand wavenumbers above the $O(^3P_2) + H(^2S)$ limit (see Fig. 1) predissociation of OH $A\ ^2\Sigma^+$ ($v = 3$) is most likely a diabatic process starting with the $1\ ^4\Sigma$ state. In the diabatic picture, the electronic Hamiltonian (without spin–orbit coupling) is diagonalized and spin–orbit interactions can cause coupling of the diabatic curves along the dissociation coordinate. If the excess energy is much larger than the spin–orbit coupling (among the $1\ ^2\Sigma^-$, $1\ ^4\Pi$, and $1\ ^4\Sigma^-$ repulsive states) there is insufficient time for the electronic and spin angular momentum to recouple at the large internuclear distance. Dissociation is then in the high-energy recoil or 'sudden' limit and takes place essentially on the initially prepared diabatic state. In this limit, the projection of the molecular wave function of the initial diabatic state onto the atomic basis states of the products determines the final product state distribution, and this distribution does not vary with the excitation energy. Because predissociation is slow compared to molecular rotation, the molecular-frame predictions given in section 2.3 below must be corrected for depolarization by rotation preceding dissociation, before projection onto the laboratory $O(^3P_J)$ (J, M_J) frame.

This journal is © the Owner Societies 2009

Phys. Chem. Chem. Phys., 2009, **11**, 4754–4760 | 4755

2.2 Depolarization of the angular anisotropy due to slow predissociation

For diatomic molecules photofragment angular distributions arising from one-photon dissociation using linearly polarized light are usually expressed[23] as

$$I(\theta) = 1/(4\pi[1 + \beta P_2(\cos\theta)]) \quad (1)$$

where β is $+2$ for a purely parallel transition ($\Delta\Omega = 0$) and $\beta = -1$ for a purely perpendicular transition ($\Delta\Omega = \pm1$), $P_2(\cos\theta)$ is the second Legendre polynomial, and θ is the angle between the fragment recoil direction and the polarization direction. The normalization factor $1/4\pi$ corresponds to unit probability for the integral of $I(\theta)$ over all solid angles. A value of β intermediate between the extremes of 2 and -1 can have several origins: a mixed parallel–perpendicular transition, depolarization due to an excited state lifetime comparable to the rotational period, or a breakdown of the axial recoil approximation. For predissociation of the OH A state, the second possibility, depolarization, is important. As mentioned previously, the low N states of A($v = 3$) have lifetimes of $\sim$200 ps, which is several orders of magnitude longer than a typical rotational period of OH.

The treatment of the anisotropy parameters resulting from predissociation of states with lifetimes comparable to, or longer than, their rotational periods has been the subject of recent studies by Houston and coworkers[24] and Kuznetsov and Vasyutinskii.[25] We use here the simulation program of ref. 24 that predicts photofragment recoil as a function of dissociation lifetime, excitation frequency, ν, rotational level and rotational constant, including both parallel and perpendicular transitions. The predicted energy dependence of β, Fig. 2, shows strong interference effects in the spatial distribution of photofragments caused by overlapping P_1, Q_1 and R_1 branch absorption features of the A $^2\Sigma^+(v' = 3, J' = 2.5, 1.5, 0.5) \leftarrow X$ $^2\Pi_{3/2}(v'' = 0, J'' = 1.5)$ transitions, and additional sharp oscillations due to interference by photoexcitation with overlapping (satellite) transitions of different parity for the Q_1,$^QP_{21}$ and R_1,$^RQ_{21}$ bands, each pair of which terminate in the same molecular axis rotation quantum number N', where $N' = 0, 1, 2$, for the P_1, Q_1, $^QP_{21}$ and R_1,$^RQ_{21}$($J'' = 1.5$) bands, respectively. In addition, the program reproduces the absorption spectrum, also shown in Fig. 2.

An accurate prediction of β from the analysis that yields Fig. 2 is complicated for the Q_1,$^QP_{21}$ band and especially the R_1,$^RQ_{21}$ band by the fact that the experimental value of the laser bandwidth ($\sim$1 cm^{-1}) is comparable to the range over which β widely oscillates. We extract an average value of β for the region covering the full width at half maximum of the absorption peak, and obtain $\beta(P_1(1.5)) = 0.0$, $\beta(Q_1,^QP_{21}(1.5)) = -0.35$, and $\beta(R_1,^RQ_{21}(1.5)) = 0.2$. These predicted values of β are far from the fast dissociation limit (see below) and also from the classical limit for slow predissociation[26] of $\beta = -0.25$, as is expected for the low quantum numbers ($N' = 0,1,2$) of this study. For $N' = 0$, reached by the $P_1(1.5)$ band, β is predicted to be equal to zero, as is expected for a rotationally isotropic upper state.
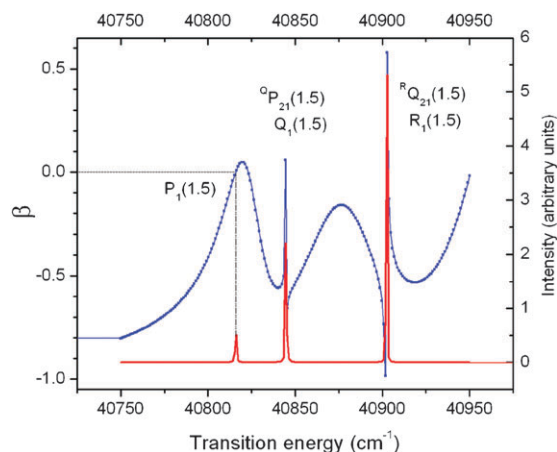
Fig. 2 Simulated absorption spectrum and β values obtained using the program of Kim *et al.*[24] Literature values of the rotational constants, spin–orbit splitting, and excited state lifetime were used, and only the $N'' = 1$ rotational state of the $^2\Pi_{3/2}$ ground electronic state is assumed to be populated. Note that β is measurable only where absorption is significant.

2.3 Molecular body-fixed frame polarization of O(^{3}P$_j$)

In the sudden recoil limit, the probability $P_{j\omega}$ of finding an O(^{3}P$_{j=0,1,2}$) atom in the (j,ω) quantum state is given in the molecular body-fixed (j,ω) frame by the projection

$$P_{j\omega} = \sum_{\omega_H} |\langle j\omega\, j_H\omega_H|L\Lambda S\Sigma\rangle|^2, \quad (2)$$

where $L = 1$, $\Lambda = 0$, $S = \frac{3}{2}$ and $\Sigma = \frac{3}{2}, \frac{1}{2}$ are the asymptotic electronic orbital angular momentum, its projection on the molecular axis, electronic spin, and spin projection quantum number, of the 1 $^4\Sigma^-$ state, respectively. The j_H and ω_H indicate the total electronic angular momentum and angular momentum projection quantum number of the hydrogen (oxygen) fragments defined with respect to the interatomic axis. Assuming spin–orbit coupling is the main predissociation mechanism, the projection of the total angular momentum on the molecular axis $\Omega = \Lambda + \Sigma = 1/2$ is preserved, so we consider only the contribution from $\Sigma = \Omega - \Lambda = 1/2$. The matrix element is computed by:

$$\langle j\omega\, j_H\omega_H|L\Lambda S\Sigma\rangle$$
$$= (-1)^{L+s+j_H}\sqrt{(2j+1)(2S+1)}$$
$$\times \sum_k (-1)^k \langle j\omega\, j_H\omega_H|k\Omega\rangle\langle L\Lambda S\Sigma|k\Omega\rangle \begin{Bmatrix} k & S & L \\ s & j & j_H \end{Bmatrix}, \quad (3)$$

where s is the spin quantum number of the oxygen fragment, and $\Omega = \Lambda + \Sigma$.

The angular distribution of a (simulated) oxygen ion image when the (linear) polarization of the detection and dissociation lasers is parallel can be expanded in ordinary Legendre polynomials P_k:

$$I_j(\theta) = \sum_{k=0,2,4} c_k(j)\, P_k(\cos\theta), \quad (4)$$

where the expansion coefficients c_k for OH photodissociation in the sudden limit (assuming axial recoil) are given by:

$$c_0(j) = P_j [1 + \tfrac{1}{5} \beta \bar{\rho}_0^{(2)}(j) I_2(j)] \qquad (5)$$

$$c_2(j) = P_j \left[\beta + \bar{\rho}_0^{(2)}(j) \ I_2(j) \left(1 + \tfrac{2}{7} \beta \right) \right] \qquad (6)$$

$$c_4(j) = P_j \frac{18}{35} P_j \beta \bar{\rho}_0^{(2)}(j) \ I_2(j), \qquad (7)$$

where P_j are the oxygen atomic fine structure branching ratios, $P_j = \sum_\omega P_{j\omega}$. These expressions follow from the paper by van Vroonhoven and Groenenboom:[27] setting $l_b = 0$ in their eqn (5) gives our present eqn (3). Eqn (4)–(7) result from eqn (31) and (32) of Ref. 27 by restricting the sum over molecular states $i\Omega$ to a single term, i.e., set $r_{i\Omega} = 1$ and $\beta_{i\Omega} = \beta$. The $\bar{\rho}_0^{(2)}(j) = \rho_0^{(2)}(j)/\rho_0^{(0)}(j)$ are the normalized irreducible components of the reduced density matrix for the oxygen fragment in the molecule-fixed frame, and:

$$\rho_0^k(j) = P_j^{-1} \sum_\omega (-1)^{j-\omega} \langle j\omega \ j -\omega | k0 \rangle P_{j\omega}. \qquad (8)$$

The $I_2(j)$ in eqn (5)–(7) are the relative absorption intensities for the $(2 + 1)$ REMPI oxygen detection scheme as defined by Mo et al.,[28] and computed by van Vroonhoven and Groenenboom.[27] We have $I_2 (0) = 0$, $I_2 (1) = 2^{-1/2}$, and $I_2(2) = -\sqrt{7/10}$. The results are summarized in Table 1. The expected recoil anisotropy parameters under fast (compared to rotation) dissociation with $\beta = -1$, which is given by[27] $\beta_j^{calc} = c_2(j)/c_0(j)$ and $\gamma_j^{calc} = c_4(j)/c_0(j)$, are also shown in Table 1.

Table 1 shows that the O^3P_j $(j = 2:1:0)$ branching ratios favors O^3P_2, but the production of O^3P_0 is larger than that of O^3P_1. Note that alignment effects are not possible for the $j_H = 1/2$ H/D (^2S) atom. As required for states with $j = 0$, the O^3P_0 channel has no orientation or alignment and yields the expected $\beta_0 = -1$ for a $\Sigma \leftarrow \Pi$ excitation and fast dissociation compared to rotation.

2.4 Lab-frame angular distributions

The predicted laboratory angular distribution parameters β_j^{calc} and γ_j^{calc} for $O(^3P_J)$ $(J = 0,1,2)$ detection obtained by combining the values for depolarization effects on the angular anisotropy for the $N' = 0, 1,$ and 2 states and the $O(^3P_J)$

Table 1 Molecular frame oxygen branching ratios distributions, $P_{j\omega}$ eqn (2), and the fragment anisotropy (β_j^{calc}) and alignment (γ_j^{calc}) parameters for direct dissociation (i.e. axial recoil) of the OH 1 $^4\Sigma^-$ state, computed in the diabatic (sudden recoil) limit[12,16] for different fine structure states (j) of the oxygen fragment when using a linearly polarized laser for REMPI detection of the $O(^3P_J)$ atom. Note that fast dissociation (compared to rotation) is not valid for OH A state predissociation, but is included here for comparison with results discussed in section 2.4 for slow predissociation

		$|\omega|$			β_j^{calc} fast	γ_j^{calc} fast
j	P_j	0	1	2	dissociation	dissociation
0	4/18	2/9			−1	0
1	3/18	0	1/6		−5/7	−2/7
2	11/18	4/9	1/6	0	−20/43	−23/43

Table 2 Predicted angular distribution parameters β_j^{calc} and γ_j^{calc} for $O(^3P_{2,1,0})$ images from the predissociation of OH in individual rotor levels of the $A \ ^2\Sigma^+$ ($v' = 3$, $N' = 0, 1, 2$) state

	$O(^3P_2)$		$O(^3P_1)$		$O(^3P_0)$	
Transition	β_2^{calc}	γ_2^{calc}	β_1^{calc}	γ_1^{calc}	β_0^{calc}	γ_0^{calc}
$P_1(1.5)$	0.7	0	0.5	0	0	0
$^QP_{21},Q_1(1.5)$	0.30	−0.13	0.11	−0.09	−0.35	0
$^RQ_{21},R_1(1.5)$	0.91	0.07	0.71	0.05	0.2	0

polarization sensitivity factors for a linearly polarized ionization laser are listed in Table 2. These values are obtained by first computing the molecular axis distribution using the predicted values of β from the depolarization analysis, combining these with molecular frame data for the atom polarization distributions (Table 1), and then combining this data with the laser polarization sensitivity factors for the REMPI process.

Branching ratios for the O^3P_J $(J = 0, 1, 2)$ channels are also measured in this work using a linearly polarized detection laser. Because the product atoms are also polarized, the total yield signal will be slightly biased, depending on the direction of the detection laser polarization. Using the predicted angular distributions from Table 2, we calculated correction factors for the case of the detection laser polarization aligned parallel to the detector face. For all combinations of predissociation of $N' = 0, 1, 2$ and O^3P_J $(J = 0, 1, 2)$ detection, the correction factors are less than 7%. These small corrections are included in the following data analysis.

3. Experimental method

A detailed description of our velocity-map imaging apparatus has been given in previous publications.[1,2] In short, the OH beam was produced using a pulsed discharge source of the pulsed H_2O beam seeded in Ar. An electrostatic hexapole lens, without a beam stop, was used to select and focus the pulsed and skimmed supersonic beam of OH in the $J = 3/2$, $|M_J| = 3/2$ state upper Λ-doublet of f-symmetry to the laser interaction region. When the molecules enter the electric field of the velocity-map imaging lens, partial orientation and alignment of the parent OH molecule is possible. Experiment and analysis showed that the parent molecule alignment effects are quite small, due to the admixture of $J = 3/2$, $|M_J| = 1/2$ molecules (which have opposite alignment effects compared to the $J = 3/2$, $|M_J| = 3/2$ state) in the molecular beam under our condition where a large repeller plate hole is used. The hexapole was mainly used for optimizing the experimental conditions, and then set to zero for the reported measurements in order to avoid any complications due to partial OH orientation and alignment.

The OH beam was directed along the axis of the TOF mass spectrometer and crossed at a right angle by the counter-propagating photolysis and probe laser beams between the repeller and extractor velocity-mapping electrodes. The vertically polarized (polarization direction perpendicular to the TOF axis and parallel to the detector face) dissociation laser was focused on the OH molecular beam by a 20 cm focal length lens and the probe laser light was focused by a 9 cm

focal length lens with vertical polarization direction (perpendicular to the TOF and parallel to the detector face) or perpendicular polarization direction (parallel to the TOF and perpendicular to the detector surface). Rotation of the detection laser polarization between vertical and horizontal polarizations was carried out using a Berek's compensator.

The ~ 245 nm photodissociation laser light (~ 0.4 mJ per pulse) was generated by frequency tripling (with a combination of KDP and BBO crystals) the output of a dye laser (Spectra Physics Quanta Ray PDL-2, LDS 750 dye) pumped by a frequency-doubled Nd:YAG laser (Spectra Physics Quanta Ray DCR-11). A single rovibronic level of the excited OH $A\,^2\Sigma^+$ state is prepared by tuning the photo-dissociation laser wavelength to the $P_1(1.5)$, $Q_1,^QP_{21}(1.5)$ and $R_1,^RQ_{21}(1.5)$ transitions at the vacuum wavelengths 245.003 nm, 244.830 nm, and 244.484 nm, respectively. $O(^3P_{2,1,0})$ product detection is achieved by two-photon excitation to the $O(2p^33p^1, {}^3P_J)$ states using vacuum wavelengths of 225.654, 226.059 and 226.233 nm for $J = 2, 1, 0$, respectively, and monitored by subsequent ionization in a two-photon resonant three-photon ionization [(2 + 1) REMPI] process.

This 226 nm radiation (~ 0.8 mJ per pulse) was generated by means of a frequency doubled (with a BBO crystal) dye laser (Continuum TDL60, Coumarin 47 dye) pumped by a frequency-tripled Nd:YAG laser (Continuum Surelite), and overlapped in time with the photolysis pulse.

O^+ ions produced by REMPI of $O(^3P_J)$ were extracted from the ionization region into the grounded time-of-flight tube by the electric field of the velocity-mapping lens and crushed onto a two-dimensional microchannel plate/phosphor screen detector read by a CCD camera. Mass selectivity was achieved by increasing the gain of the detector as the O^+ ions arrive. Typically, 10 000 laser shots were used to produce the final 2D raw image.
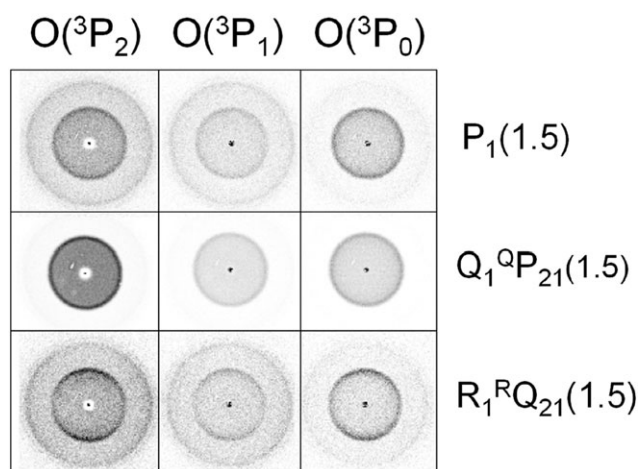
Fig. 3 Raw $O(^3P_{2,1,0})$ images produced by (2 + 1) REMPI at ~ 226 nm of the $O(^3P_J)$ atom fragments coming from the electronic pre-dissociation of OH of $A\,^2\Sigma^+$ ($v' = 3$) state via the transitions $P_1(1.5)$, $Q_1,^QP_{21}(1.5)$ and $R_1,^RQ_{21}(1.5)$. All images are taken with the polarization direction of both the photodissociation and probe laser aligned parallel to the detector face, which is the vertical axis in the figure. Darker regions correspond to higher signal levels.

4. Experimental results and analysis

4.1 Description of images

In Fig. 3 a set of representative raw O^+ images of $O(^3P_J)$ from the pre-dissociation of OH $A\,^2\Sigma^+$ ($v' = 3$) populated via three $A-X$ transitions ($P_1(1.5)$, $Q_1,^QP_{21}(1.5)$ and $R_1,^RQ_{21}(1.5)$) are shown. This set of images was taken in one day, the full angular distribution and branching ratio information was extracted from a much larger set of images. The center of each image corresponds to zero-velocity $O(^3P_J)$ atoms formed and cooled in the discharge source and signals at a larger distance from the image center arise from photofragments with non-zero velocities. Two rings are seen in each image, the main, inner, ring arises from the pre-dissociation of OH $A\,^2\Sigma^+$ ($v' = 3$) while the outer ring is from the ~ 226 nm probe laser only and corresponds to one-photon dissociation of OH populated in high vibrational levels of the $X\,^2\Pi$ ground electronic via the repulsive $1\,^2\Sigma^-$ state.[1,2]

Under our experimental conditions of high repeller voltage and wide mass gate, the images are fully crushed, i.e., no slicing should be taking place. These images are thus 2D projections of the 3D velocity distributions, with the polarization vector of the photodissociation laser and probe laser maintained parallel to the detector face and thus along the vertical axis of Fig. 3. We analyze these parallel polarization raw images using the Basex inversion program.[29]

Two main trends are apparent in these images. First, the $O(^3P_2)$ images are more intense than the $O(^3P_0)$ images, which are themselves more intense than the $O(^3P_1)$ images. Second, the $R_1\,^RQ_{21}(1.5)$ images are noticeably anisotropic with a parallel character (positive β value) while the $P_1(1.5)$ and $Q_1,^QP_{21}(1.5)$ images are closer to isotropic. Images taken with both lasers polarized along the time-of-flight axis (perpendicular to the detector face) yielded isotropic rings, which confirmed the homogeneity of the detector, while images taken with the dissociation laser parallel and the probe laser perpendicular to the detector face showed for $O(^3P_0)$ atoms the same signal as the parallel–parallel configuration. The result of alignment effects for $O(^3P_{2,1})$ atoms discussed in section 4.3 were independently confirmed on a qualitative level using this parallel–perpendicular geometry, but a direct analysis of the atomic polarization by subtraction of parallel–parallel from parallel–perpendicular polarized images[8] was not reliable due to the limited signal-to-noise ratio of the images.

4.2 $O(^3P_J)$ fine structure branching ratios

Branching ratios for the $O(^3P_J, J = 2, 1, 0)$ fine structure states are obtained by integrating the signal of the raw $O(^3P_J)$

Table 3 Experimental fine-structure branching ratios of $O(^3P_J)$, $J = 2,1,0$ atom fragments arising from the predissociation of the OH $A\,^2\Sigma^+$ ($v' = 3$) state. The uncertainty (one standard deviation) for each value is ± 0.07

Transition	$O(^3P_2)$	$O(^3P_1)$	$O(^3P_0)$
$P_1(1.5)$	0.58	0.20	0.22
$Q_1,^QP_{21}(1.5)$	0.65	0.16	0.19
$R_1,^RQ_{21}(1.5)$	0.58	0.19	0.23

images. These images were taken using a constant pulse energy for both the excitation laser, used to populate the A($v' = 3$) state, and the detection laser, used to ionize $O(^3P_J)$ atoms. The experimental fine-structure branching ratios are then adjusted with the previously mentioned correction factors for using a linearly polarized ionization laser. Results from several sets of images taken during different measurement sessions are averaged, and reported in Table 3. Our data has a much larger range of uncertainty (± 0.07 for one standard deviation) than the Rydberg tagging data of Zhou et al.,[3] where the three co-partner $O(^3P_J)$ peaks are clearly resolved in their H atom TOF spectrum. Zhou et al.[3] reported an $O(^3P_J)$ branching ratio of $J = 2:1:0 = (0.676 \pm 0.010 : 0.138 \pm 0.013 : 0.186 \pm 0.017)$ for the $P_1(1.5)$ branch, while we obtain $0.58 : 0.20 : 0.22 \pm 0.07$ for the same transition, The two results agree reasonably well within our error range. In our experiment the most difficult challenge is maintaining the same overlap of the excitation and probe lasers in time and space for three different $O(^3P_J)$ probe laser wavelength conditions, while maintaining constant laser pulse energy, wavelength, and laser bandwidth and molecular beam conditions. For this reason we expect that the $O(^3P_J)$ branching ratio data of Zhou et al.[3] is more reliable than our two-color data.

4.3 Angular distribution and alignment

The experimentally determined angular distribution parameters (β_J^{exp}, γ_J^{exp}) [as defined in eqn (5)] obtained from our images are given in Table 4, and plotted along with the theoretical values of Table 2 in Fig. 4. As seen in Table 4,
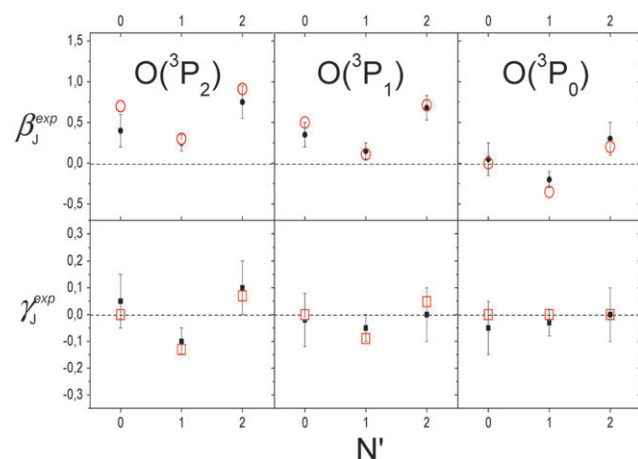
Fig. 4 Experimentally determined angular distribution parameters (β_{exp}, γ_{exp}) from the $O(^3P_{2,1,0})$ images (solid circles and squares, respectively) and the sudden-limit predictions (β_{theory}, γ_{theory}) (open circles and squares) from Table 2.

the γ_J^{exp} values for the $O(^3P_0)$ images are indeed, within the experimental uncertainty, equal to zero. In general, our data agrees remarkably well with the predictions from the sudden limit model combined with the depolarization analysis shown in Fig. 2. The predicted values are sensitive to the value of β extracted from the depolarization analysis, which appears directly as the $O(^3P_0)$ (alignment-free) β_0^{exp} value in Table 2. Considering the rather simple theoretical model and the many experimental uncertainties, the agreement between theory and experiment is quite good.

5. Discussion and conclusions

The $A\,^2\Sigma^+$ ($v' = 3$, $N' = 0$) state predissociates predominantly via the $^4\Sigma^-$ state, as shown by the studies of $A\,^2\Sigma^+$ state predissociation rates.[10,14–16] Parlant and Yarkony[16] have shown that the $^4\Sigma^-$ state should have the dominant effect on the branching fractions for A($v' = 2$ and 3, $N' = 0$) and also that passage through the $^4\Sigma^-$ state channel favors $O(^3P_J)$ atom products in $J = 2$ over $J = 0, 1$. In the sudden (diabatic) limit, single-state fine-structure $O(^3P_J)$ branching fractions for the $^4\Sigma^-$ channel [the single-state approximation includes only one spin–orbit coupling (e.g. $A\,^2\Sigma^+ \leftrightarrow {}^4\Sigma^-$) with all remaining spin–orbit couplings and all intrashell interactions set to zero] are $O(^3P_{2,1,0}) = 0.611 : 0.167 : 0.222$.[16] A fully quantum calculation (multichannel scattering including all the non-adiabatic interactions from the Franck–Condon to asymptotic region) predicts $O(^3P_{2,1,0}) = 0.675 : 0.141 : 0.184$[16] and the experimental data from Zhang and coworkers[3] gives very similar values ($0.676 : 0.138 : 0.186$). It should also be noted that the sudden-limit single-state branching fractions for the $^4\Sigma^-$ state,[12] the predicted spin–orbit branching ratios using the full quantum calculation,[16] and the experimental data from Zhang and coworkers[3] all show the same order in signal strength $O(^3P_2) > O(^3P_0) > O(^3P_1)$. Our experimental data showed this same order, but with larger error bars.

Our experimentally observed $O(^3P_J)$ angular distribution parameters for OH photo-predissociation are compared with sudden limit theory in Fig. 4. In order to make this comparison we have combined predictions of the depolarization of the product angular distribution due to slow predissociation by Houston and coworkers[24] (Fig. 2) with a one-state sudden-limit analysis for predicting the molecular frame atomic alignment parameters. This slow predissociation model considers only coherence effects in the optical excitation step, separately from coherence effects in product formation. While quite simplistic, it is clear from Fig. 4 that the fine-structure β_j^{exp} and γ_j^{exp} parameters for $O(^3P_{2,1,0})$ fragments are in good agreement with the predictions from this approach.

Table 4 Experimentally determined angular distribution parameters β_J^{exp} and γ_J^{exp} from the background subtracted $O(^3P_{2,1,0})$ images. Error bars are given in parenthesis

Transition	$O(^3P_2)$		$O(^3P_1)$		$O(^3P_0)$	
	β_2^{exp}	γ_2^{exp}	β_1^{exp}	γ_1^{exp}	β_0^{exp}	γ_0^{exp}
$P_1(1.5)$	0.40(20)	0.05(10)	0.35(15)	−0.02(10)	0.05(20)	−0.05(10)
$Q_1, {}^QP_{21}(1.5)$	0.25(10)	−0.10(05)	0.15(10)	−0.05(05)	−0.20(10)	−0.03(05)
$R_1, {}^RQ_{21}(1.5)$	0.75(20)	0.10(10)	0.68(15)	0.00(10)	0.30(20)	0.00(10)

This journal is © the Owner Societies 2009

Phys. Chem. Chem. Phys., 2009, **11**, 4754–4760 | 4759

In general, the uncertainty in our experimental data, especially for the fine-structure branching ratios, is higher than desired. In order to improve the data quality for a more stringent test of the validity of the sudden limit model, an alternative source of OH will probably be necessary. Background due to photodissociation of vibrationally excited water molecules and to other species formed in the discharge is a major contributor to the experimental uncertainty.

We attempted a study of the predissociation of the $v' = 4$ vibrational level using the $A\,^2\Sigma^+$ ($v' = 4$, N', J', F_1) ← $X\,^2\Pi_{3/2}$ ($v'' = 0$, $N'' = 1$, $J'' = 3/2$, F_1) transition at $\sim$232 nm. The signal-to-noise for detection of $O(^3P_J)$ dissociation products at 232 nm, however, was too low in our apparatus to yield useful data, due in part to extra background at this wavelength from 'hot' water produced in the discharge source, as mentioned above. The A($v = 4$) ← X($v = 0$) transition has a much lower Franck–Condon overlap factor[30] ($\Delta v = 4$:(4,0) $= 6.6 \times 10^{-5}$) than that for the transitions to $v' = 3$ ($\Delta v = 3$:(3,0) $= 6.4 \times 10^{-4}$). Another possibility now under investigation is excitation of the $v'' = 1$ component of the beam ($\sim$5% populated) via the $\Delta v = 3$:(4,1) transition, which has a Franck–Condon factor of 3.19×10^{-3}.

We have also recently reported a study of A-state ($v = 0, 1$, and 2) predissociation of the isovalent SH/SD molecules.[7] For the predissociation process SH and OH differ most in the position of the A($v = 0$) state with respect to the first dissociation limit. In SH even the lowest rotational levels of A($v = 0$) show predissociation, while in OH only the higher rotational levels of A($v = 2$) begin to show appreciable predissociation rates. For OH all predissociative levels are thus significantly above the dissociation limit and a sudden limit model is valid. For SH, and especially SD, the A($v = 0$) level shows a much more adiabatic dissociation behavior where $S(^3P_2)$ is almost the only observable product. For the ($v = 2$) vibrational level of SH there is evidence in the $S(^3P_J)$ branching ratios for a contribution from the $^2\Sigma^-$ repulsive state in addition to the $^4\Sigma^-$ state. In terms of product polarization, OH is also simpler in that sudden-limit model with depolarization appears to account quite well for the observed polarization behavior. For SH a quantitative polarization analysis is first of all more difficult due to a partial splitting of the upper state levels in the REMPI process, and the analysis shows a rather constant polarization behavior, described by neither the adiabatic or sudden limit model, over the full dissociation energy range studied.[7] We can thus conclude that predissociation of OH A($v = 3$, $N' = 0, 1, 2$) can be described by the single-state sudden-limit model, within the accuracy of our data, while SH/SD, due to the different positioning of the A(v) levels with respect to the dissociation limit and the repulsive electronic states, shows a more complex behavior.

Acknowledgements

References

1 D. Č. Radenović, A. J. A. Van Roij, D. A. Chestakov, A. T. J. B. Eppink, J. J. ter Meulen, D. H. Parker, M. P. J. Van der Loo, G. C. Groenenboom, M. E. Greenslade and M. I. Lester, J. Chem. Phys., 2003, **119**, 9341.
2 Dragana Č. Radenović, André. J. A. van Roij, Shiou-Min Wu, J. J. ter Meulen, David H. Parker, Mark. P. J. van der Loo, Liesbeth M. C. Janssen and Gerrit C. Groenenboom, Mol. Phys., 2008, **106**, 557.
3 W. Zhou, Y. Yuan and J. Zhang, J. Chem. Phys., 2003, **119** 9989.
4 K. Schreel and J. J. ter Meulen, J. Phys. Chem. A, 1997, **101** 7639.
5 A. T. J. B. Eppink and D. H. Parker, Rev. Sci. Instrum., 1997, **68**, 3477.
6 A. P. Clark, M. Brouard, F. Quadrini and C. Vallance, PCCP, 2006, **8**, 5591.
7 R. A. Rose, A. J. Orr-Ewing, C.-H. Yang, K. Vidma, G. C. Groenenboom and D. H. Parker, J. Chem. Phys., 2009, **130**, 034307.
8 E. R. Wouters, M. Ahmed, D. S. Peterka, A. S. Bracker, A. G. Suits and O. S. Vasyutinskii, in Imaging in Chemical Dynamics, ed. A. G. Suits and R. E. Continetti, American Chemical Society, Washington, DC, 2001, pp. 238.
9 M. P. J. Van der Loo and G. C. Groenenboom, J. Chem. Phys., 2005, **123**, 074310.
10 M. L. Sink, A. D. Banddrauk and R. Lefebvre, J. Chem. Phys., 1980, **73**, 4451.
11 E. F. Dishoeck and A. Dalgarno, J. Chem. Phys., 1983, **79** 873.
12 S. Y. Lee and K. F. Freed, J. Chem. Phys., 1987, **87**, 5772.
13 S. Y. Lee, J. Chem. Phys., 1995, **103**, 3501.
14 C. Kalyanaraman and N. Sathyamurthy, Chem. Phys., 1994, **187**, 219.
15 D. R. Yarkony, J. Chem. Phys., 1992, **97**, 1838.
16 G. Parlant and D. R. Yarkony, J. Chem. Phys., 1999, **110**, 363.
17 J. Brzozowski, P. Erman and M. Lyyra, Phys. Scr., 1978, **17**, 507.
18 J. A. Gray and R. L. Farrow, J. Chem. Phys., 1991, **95**, 7054.
19 D. E. Heard, D. R. Crosley, J. B. Jeffries, G. P. Smith and A. Hirano, J. Chem. Phys., 1992, **96**, 4366.
20 J. J. L. Spaanjaars, J. J. ter Meulen and G. Meijer, J. Chem. Phys., 1997, **107**, 2242.
21 E. L. Derro, I. B. Pollack, L. P. Dempsey, M. E. Greenslade, Y. Lei, D. Č. Radenović and M. I. Lester, J. Chem. Phys., 2005, **122**, 244313.
22 R. A. Copeland, J. B. Jeffries and D. R. Crosley, J. Mol. Spectrosc., 1990, **143**, 183.
23 R. N. Zare and D. R. Herschbach, Proc. IEEE, 1963, **51**, 173.
24 H. Kim, K. S. Dooley, S. W. North Gregory E. Hall and P. L. Houston, J. Chem. Phys., 2006, **125**, 133316.
25 V. V. Kuznetsov and O. S. Vasyutinskii, J. Chem. Phys., 2007, **127**, 044308.
26 C. Jonah, J. Chem. Phys., 1971, **55**, 1915.
27 M. C. G. N. van Vroonhoven and G. C. Groenenboom, J. Chem. Phys., 2002, **116**, 1965.
28 Y. Mo, H. Katayanagi and T. Suzuki, J. Chem. Phys., 1998, **109**, 4691.
29 V. Dribinski, A. Ossadtchi, V. A. Mandelshtam and H. Reisler, Rev. Sci. Instrum., 2002, **73**, 2634.
30 J. Luque and D. R. Crosley, J. Chem. Phys., 1998, **109**, 439.

4760 | Phys. Chem. Chem. Phys., 2009, **11**, 4754–4760

This journal is © the Owner Societies 2009